



A 2D continuous-discrete mixed seepage model considering the fluid exchange and the pore pressure discontinuity across the fracture for simulating fluid-driven fracturing

Chengzeng Yan^{1,2} · Yuxin Wang¹ · Xin Xie¹ · Sajid Ali¹ · Zhigang Sheng³

Received: 28 April 2022 / Accepted: 9 June 2023 / Published online: 18 July 2023
© The Author(s), under exclusive licence to Springer-Verlag GmbH Germany, part of Springer Nature 2023

Abstract

Based on the finite-discrete element method (FDEM), this paper proposes a continuous-discrete mixed seepage model that considers the fluid exchange and the pore pressure discontinuity across the fracture. The continuous-discrete seepage model uses the cubic law to express the fluid flow in the fracture and Darcy's law to describe the pore seepage in the rock matrix. Combining the continuous-discrete mixed seepage model with the FDEM, a hydro-mechanical coupling model is constructed to solve fluid-driven fracturing of a rock mass. The continuous-discrete seepage model and hydro-mechanical coupling model update the node sharing relationship of triangular elements on two sides of the fracture during fracture propagation which sufficiently consider the influence of the fracture propagation on the pore seepage. In this paper, the analytical solutions are used to verify the model's accuracy with the help of four examples. In addition, the hydro-mechanical coupling model is used to simulate a hydraulic fracturing problem for rock mass involving a complex fracture network. According to the simulation results, this hydro-mechanical coupling model can catch fracture initiation, propagation, the interaction between hydraulic fractures and discrete fracture, as well as the evolution of pore pressure and fracture pressure.

Keywords Finite discrete element method (FDEM) · Fluid-driven fracturing · Fracture-pore mixed seepage · Hydraulic fracturing · KGD

1 Introduction

The coupling of two processes means that one process affects the occurrence and development of another process. The research on the hydro-mechanical coupling of porous media began in the 1940s, and Terzaghi first proposed the concept of effective stress when studying soil mechanics. Then, Biot studied the hydro-mechanical coupling

problems in soil consolidation and foundation subsidence. Since then, the theory has been applied to study the open or close of fractures or joints in the rock mass, hydraulic fracturing, and earthquakes triggered by fluid injection.

Many problems in geotechnical engineering are related to hydro-mechanical coupling. For example, landslides and slopes failure, dam foundations failure, stability of underground excavation, stability of boreholes in oil and gas extraction, hydraulic fracturing, geothermal mining, and coal mining are all related to rock fracturing under the effect of hydro-mechanical coupling. Therefore, building a seepage and hydro-mechanical coupling model considering rock fracturing is of great significance for solving the engineering problems related to hydro-mechanical coupling that widely exist in geotechnical engineering.

Moreover, many authors have investigated this issue, which is summarized in three parts below: (1) computational method for seepage in complex fractured rock mass;

✉ Chengzeng Yan
yancz@cug.edu.cn

¹ Faculty of Engineering, China University of Geosciences, Wuhan 430074, China

² National Center for International Research on Deep Earth Drilling and Resource Development, China University of Geosciences, Wuhan 430074, China

³ Institute of Disaster Prevention, College Street in Yanjiao Quarter, East of Beijing 101601, China

(2) hydro-mechanical coupling analytical model; (3) hydro-mechanical coupling numerical model.

1.1 Computational method for seepage in a complex fractured rock mass

The computational method for seepage in the complex fractured rock mass is relatively advanced. The fracture and pore seepage can be considered directly or indirectly, and they can be divided into the equivalent continuum model (ECM) [42, 60], dual-porosity model (Dual-Porosity Model) [18, 43], discrete fracture network model (DFN) [13, 33], and discrete fracture-matrix model (DFM) [17]. Among these, the discrete fracture network model (DFN) employs the cubic law to describe the fluid flow of fractures in the rock mass through a more comprehensive modeling of the fractures. However, the permeability of rock itself is ignored in DFN. The ECM cannot accurately characterize the fractures, which does not directly model the fracture seepage. Instead, the fracture permeability is equivalent to the entire medium. Therefore, it is difficult to characterize the preferential conductivity of the local area at the fracture. In the dual-porosity model, the fractured medium is regarded as a medium whose permeability is much larger than that of the rock matrix, so the preferential conductivity of the fracture is considered. However, the pore pressure across the fracture is continuous because the elements on both sides of the fracture share nodes. Since fractures usually are very narrow, the mesh needs to be very dense. The discrete fracture-matrix model absorbs the advantages of the discrete fracture network model to describe the fracture seepage accurately. It also considers the pore seepage of the rock matrix [21, 23]. The above research mainly limits pure seepage problems in fractured rock masses and rarely considers hydro-mechanical coupling and fluid-driven fracturing of a rock mass.

1.2 Hydro-mechanical coupling analytical model

The classical coupling model of porous media like rock and soil can be derived from Biot's consolidation theory. Another significant force that drives the research of rock mass fracturing under hydro-mechanical coupling is the widespread use of hydraulic fracturing technologies in oil and gas production. In response to this problem, researchers have established a series of analytical models for hydraulic fracturings, such as the PKN model [38, 39], KGD model [15, 24], and the axisymmetric penny-shaped model [1]. Under some simplified assumptions, Khris-tianovic [15, 24] proposed a hydraulic fracturing model, namely the KGD model, for continuous, uniform, and isotropic linear elastic media. According to this model, the fracture tip process controls fracture propagation;

therefore, it is more suitable for the formation of fractures whose height is much greater than the fracture length. The asymptotic solution of the KGD model shows that the fluid-driven fracture propagation process is mainly controlled by two competing mechanisms: energy dissipation and fluid storage. Energy dissipation includes fracture propagation and the viscous flow of fracturing fluid in fractures. The fluid storage includes fluid storage in fractures and fluid loss in porous media. Detournay [9] has done an in-depth study on the mechanism of energy dissipation and found that there are four main types of energy dissipation: storage-toughness, storage-viscosity, leak-off-toughness, and leak-off-viscosity.

In the past few decades, scholars have studied the asymptotic solution of KGD. Adachi, Detournay [3] derived a self-similar solution to the 2D hydraulic fracturing problem driven by a power-law fluid. Garagash, Detournay [14] obtained a similar solution for a fluid-driven fracture propagating in the viscous-dominated zone in the case of plane strain. Bungler et al. [5] derive the small-time asymptotic solution and the large-time asymptotic solution, respectively, under the conditions of fluid storage in fractures or fluid permeability in rocks. Although these models have certain limitations, they can be used as benchmarks for numerical simulations and to analyze the effects of different parameters on hydraulic fracturing.

1.3 Hydro-mechanical coupling numerical model

To conduct a more in-depth study of hydraulic fracturing, many scholars have built different numerical models and verified the numerical models through the KGD model. Lecampion et al. [26] reviewed the basics of the hydraulic fracture problem and its intrinsic peculiarities and the benefits and limitations of the recently developed continuum and meso-scale numerical methods. Various numerical models based on the finite element method are widely used for hydraulic fracturing simulation. Carrier, Granet [8] established a hydro-mechanical coupling model in the finite element method to study the four energy dissipation mechanisms in the fracturing process. Manzoli et al. [32] proposed an approach for simulating the formation and propagation of fractures in rocks based on high aspect ratio (HAR) elements, which uses standard finite element techniques to deal with discontinuities in porous media. Hunsweck et al. [19] proposed a finite element algorithm to study the problem of hydraulic fracture propagation in a plane strain impermeable formation, which can simulate fluid leakage phenomena with non-Newtonian rheology. Compared with the classic finite element method, the fracture propagation in the extended finite element method can be independent of the computational mesh and simulate the propagation of fractures in any direction. Yan et al.

[63] proposed a new hydromechanical coupling stratified simulation method for fractured shale gas reservoirs, which uses the finite difference method and stable extended finite element method to discretize the seepage model and geomechanical model, and a sequential implicit method is adopted for solving the model. Zhang et al. [78] proposed a new formula for the stability of anisotropic double-porosity media based on the smooth finite element method (NS-FEM) and realized the coupling between double porosity flow and deformation formulation. Li et al. [28] proposed a multi-fracture coupling simulation algorithm based on extended finite element that does not require the introduction of a leak-off coefficient to describe the fluid loss phenomenon and to pre-determine the direction of fracture propagation. Dugdale [11] and Barenblatt [4] first proposed a cohesive zone model, which provides a new approach for simulating hydraulic fracturing. Mahdi Haddad, Sepehrnoori [16] proposed a cohesive zone model (CZM) based on extended finite elements, which can effectively simulate the extension of fractures in any direction and consider the fluid loss in the rock matrix. Li et al. [29] used a 2D pore pressure cohesive zone model to simulate hydraulic fracture propagation in naturally fractured formations. However, this model does not consider the influence of fluid loss into the rock matrix on hydraulic fracturing. Salimzadeh et al. [41] proposed a fully coupled three-dimensional finite element model for hydraulic fracturing in permeable rocks.

In addition to the finite element method, the discrete element method has been used to simulate hydraulic fracturing in recent years. Liu et al. [31] revised the hydro-mechanical coupling model in PFC and proposed a fractured porous media permeability model to simulate the interaction between two adjacent fractures after fluid injection. Zangeneh et al. [76] used 2D discrete element code (UDEEC) to simulate the propagation of hydraulic fractures in fractured rock masses. The Voronoi subdivision scheme is used to add the necessary degrees of freedom to provide as many paths as possible for fracture propagation.

In addition, some other numerical methods, such as the displacement discontinuous method (DDM) and numerical manifold method (NMM), are also used to simulate hydraulic fracturing. Kresse et al. [25] proposed an unconventional fracture model (UFM) to simulate the propagation of fractures in naturally fractured formations, using the 2D discontinuous displacement method (DDM) to calculate the induced stress of any fracture in the rock. Xie et al. [46] improved the hydro-mechanical coupling function in the fracture mechanics modeling code (FRACOD) to simulate hydraulic fracturing. Wu et al. [45] proposed a Voronoi particles numerical manifold method based on bonding elements, which can simulate hydraulic fracture propagation from a microscopic perspective. However, this method has limitations due to the

complexity of rock microstructure and the interaction between rock microstructure and fracturing fluid. Since the cohesive zone model assumes that fractures can only propagate on the element's boundary, the propagation direction of fractures is restricted.

The finite-discrete element method (FDEM) was first conceived by Munjiza at Tohoku University Japan in 1989 and initially developed in Swansea and MIT in 1990–1992, which combines the advantages of the finite element method and discrete element method [35]. At present, three classic monographs about FDEM have published: *The Combined Finite Discrete Element Method* [34]; *Computational Mechanics of Discontinua* [36]; *Large strain Finite element method a practical course* [37], and *Computational Particle Mechanics special issue* [40] on FDEM was published in 2020. FDEM can effectively simulate the fracture and deformation of solid materials, and it is also the preferred method for simulating the fracture and fragmentation of solid materials recently [2, 27, 44, 47]. However, FDEM initially did not have a seepage calculation module and could not deal with the hydro-mechanical coupling problem. Many scholars combine FDEM with some computational fluid dynamics solvers for fluid–structure coupling calculations. For example, Lei et al. [27] combined FDEM and fluid computational software to solve the seepage-stress coupling problem in a fractured rock mass. However, it mainly considers the deformation of the rock mass and the opening or closing of fractures but does not consider the fracture initiation and propagation in the rock mass. However, this approach cannot consider a fluid loss because the pore seepage is ignored. AbuAisha et al. [2] investigated the relationship between microseismic activity and hydraulic fracture propagation using FDEM. Cao et al. [6, 7] applied FDEM to realize formation fracturing by high-energy impulsive mechanical loading and studied the empirical scaling. Ju et al. [22] used an adaptive finite discrete element method to simulate the extension of hydraulic fractures in the strata bedding interface and analyze the influence of the layered interface on the extension of hydraulic fractures. Yan et al. [52, 55–59, 62] proposed four FDEM-flow2D/3D models for simulating rock mass fracturing under hydro-mechanical coupling, which can directly perform hydro-mechanical simulation in FDEM. These models have been integrated into a GPU parallel multiphysics finite-discrete element software MultiFracS developed by Yan [70], which has been used to simulate soil desiccation cracking [53, 65, 66, 72], grouting [71], rock experimental [54], contact heat transfer and induced thermal cracking [48–51, 61, 67–69, 73–75]. The first model describes fracture seepage but not fluid loss, whereas the second model considers the surrounding rock matrix from the fracture. However, the pore seepage is equivalently represented by the fracture seepage in the

unbroken joint element. Therefore, the permeability of the rock matrix is determined by the initial aperture of the unbroken joint element. When dealing with the problem of unsteady pore seepage, this equivalent method has fluid flow hysteresis. The hydro-mechanical coupling model developed by Lisjak et al. [30] based on FDEM is the same as the second model. The third model is a fully coupled model which considers two seepage types instead of using fracture seepage to express the pore seepage. The third model overcomes the shortcomings of the first two models. However, the model cannot consider the discontinuity of pore pressure across fracture and the influence of fracture propagation on the computational mesh for pore pressure calculation. The fourth model overcomes shortcomings of the first three models. However, due to the introduction of unbroken joint elements in the pore seepage calculation of the continuous medium, the unbroken joint elements hinder the fluid exchange between the adjacent triangular elements. To make the hindrance of the joint element small enough, the exchange coefficient of the unbroken joint element is required to be $100k/(\mu L_e)$. Due to large exchange coefficient, the time step for pore seepage calculation is reduced by 100 times, which greatly reduces the efficiency of pore seepage calculation.

Therefore, a new 2D continuous-discrete mixed seepage and hydro-mechanical coupling models are established and implemented in the GPU parallel multiphysics finite-discrete element software MultiFracS. The model considers two seepage types simultaneously. The node sharing relationship of triangular elements on both sides of the fracture will be updated dynamically in the process of fracture propagation. The adjacent triangular elements on the two sides of the fracture do not share nodes. The pore pressure discontinuity across the fracture and the influence of fracture propagation on the seepage are well-considered. Thus, there is no need to add virtual unbroken joint elements. The time step for pore seepage calculation is not needed to reduce. Combining the continuous-discrete mixed seepage model with FDEM can establish a hydro-mechanical coupling model to simulate the deformation and fracturing of fracture-porous media. In addition, the hydro-mechanical coupling model has obvious advantages compared with the traditional numerical model for simulating hydraulic fracturing, which can simulate hydraulic fracturing in any complex fractured reservoir. The traditional numerical model for hydraulic fracturing can only consider simple fractures and cannot deal with the extension and intersection of complex fractures.

This paper is structured as follows. First, the existing related analytical and numerical models about seepage and hydro-mechanical coupling are introduced. Then, the details of the continuous-discrete seepage model are presented. The third section is about the basic principle of hydro-mechanical coupling, FDEM, application of fracture pressure and

pore pressure, fracture-stress-seepage coupling, and the influence of fracturing on the pore seepage computational mesh or the node shared relationship between adjacent triangular elements at the fractures. In Sect. 4, the continuous-discrete mixed seepage model and hydro-mechanical coupling model are thoroughly verified by a single fracture pore mixed seepage problem, pore seepage problem in porous media with impervious fractures, multi-fractures pore mixed seepage problems, and some hydro-mechanical coupling problems, including pore seepage-stress coupling problem (soil consolidation), fracture seepage-stress coupling problem (KGD). In the end, an application example of hydraulic fracturing is given to investigate interaction between hydraulic fractures and discrete fracture.

2 A 2D continuous-discrete seepage mixed model

2.1 Fracture seepage model

As shown in Fig. 1, when fluid flows in a fracture, a corresponding fracture pressure is exerted on both sides of the fracture. The fracture aperture increases or decreases under fracture pressure. According to the cubic law, the change of the fracture opening affects the flow rate of the fluid and the fracture pressure.

Figure 1 shows a part of the fracture network for the fracture seepage calculation. The empty area between each adjacent fracture node at the fracture represents a pathway for fluid flow in the fracture network (as shown in Fig. 1, a flow path formed by the blank empty area between fracture node $c1$ and fracture node $c2$). There is no fracture seepage in the remaining parts.

The steps to solve the flow between the two fracture nodes are first to determine the fracture pressure difference between the two fracture nodes. For fracture node $c2$, the total fracture pressure difference between fracture node $c2$ and $c1$ is:

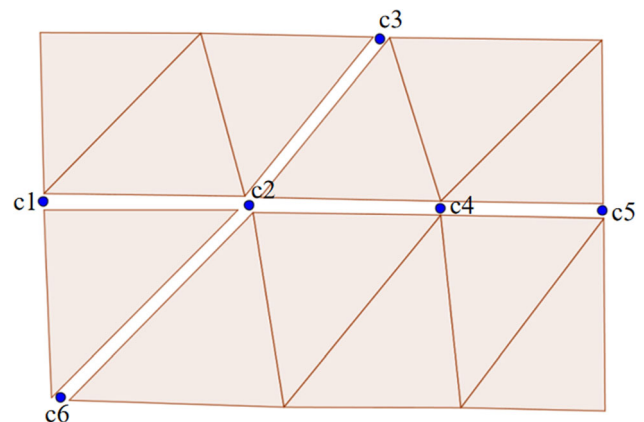


Fig. 1 Fluid flow in the fracture network

$$\Delta p = p_{c1} - p_{c2} + \rho_w g (y_{c1} - y_{c2}) \quad (1)$$

where p_2 is the fracture pressure at fracture node $c2$, p_1 is the fracture pressure at node $c1$, y_{c1} and y_{c2} is the ordinate of fracture nodes $c1$ and $c2$, respectively. Then, according to the cubic law, the flow rate of fracture node $c1$ into $c2$ can be obtained as:

$$q_{c1 \rightarrow c2} = \frac{1}{12\mu} a^3 \frac{\Delta p}{L} \quad (2)$$

where μ is the fluid viscosity coefficient, a is the average aperture of the fracture and L is the distance between two fracture nodes.

Since fracture node $c2$ is also connected to fracture nodes $c3$, $c4$, and $c6$, the flow from fracture nodes $c3$, $c4$, and $c6$ into $c2$ $q_{c3 \rightarrow c2}$, $q_{c4 \rightarrow c2}$, $q_{c6 \rightarrow c2}$ can be solved similarly. Therefore, the total flow into fracture node $c2$ is: $Q_{c2} = q_{c1 \rightarrow c2} + q_{c3 \rightarrow c2} + q_{c4 \rightarrow c2} + q_{c6 \rightarrow c2}$.

Then, the fracture pressure of fracture node 2 can be updated by:

$$p_{c2}^{t+\Delta t} = p_{c2}^t + K_w Q_{c2} \frac{\Delta t}{V} - K_w \frac{\Delta V}{V_m} \quad (3)$$

where p_{c2}^t is the fracture pressure of fracture node $c2$ at the previous time step, K_w is the bulk modulus of the fluid, and Q is the total flow into fracture node $c2$. Δt is the time step, $\Delta V = V - V_0$, $V_m = \frac{(V+V_0)}{2}$, where V is the volume of fracture node $c2$ at the current time step and V_0 and V is the volume of fracture node $c2$ at the previous time step.

2.2 Pore seepage model

According to Darcy's law, the flow velocity in the i direction can be expressed as:

$$q_i = -k_{ij} \frac{\partial \phi}{\partial x_j} \quad (4)$$

where k_{ij} is the permeability coefficient tensor, ϕ is the total head, which is defined as:

$$\phi = (p - \rho_w x_k g_k) / (\rho_w g) \quad (5)$$

where ρ_w is the fluid density, g is the modulus of the gravitational acceleration vector, and the subscript symbol g represents two components.

This paper uses a 2D mixed seepage model to discretize the fractured rock mass into a computational mesh, as shown in Fig. 2. There are no nodes on either side of the fracture shared by the adjacent triangular elements. This work established the pore seepage model. The pore pressures at pore nodes 1–18 are used to describe the pore pressure distribution of the entire medium. The topological relationship represented how to calculate the pore pressure evolution in fractured porous media.

For pore node 1 in Fig. 2, the triangular elements sharing pore node 1 have 2 triangular elements $\Delta 123$ and $\Delta 137$. Consider one of the triangular elements $\Delta 123$ as an example. Assuming that the total head distribution is a linear distribution for triangular elements and the total head gradient is constant which can be expressed as:

$$\frac{\partial \phi}{\partial x_i} = \frac{1}{A} \int_A \frac{\partial \phi}{\partial x_i} dA \quad (6)$$

According to the Gaussian divergence theorem, Eq. (6) can be written as:

$$\frac{\partial \phi}{\partial x_i} = \frac{1}{A} \int_s \phi n_i ds = \frac{1}{A} \sum_{m=1}^3 \bar{\phi}^m \epsilon_{ij} \Delta x_j^m \quad (7)$$

where A is the area of the element, $\bar{\phi}^m$ is the average pore pressure at the edge m of the triangular element, n_i is the external normal unit vector and ϵ_{ij} is a 2D permutation tensor, namely $\epsilon = \begin{pmatrix} 0 & 1 \\ -1 & 0 \end{pmatrix}$. q_i is the flow rate in the i direction and can be obtained by substituting Eq. (7) into Eq. (4):

$$q_i = -k_{ij} \left(\frac{1}{A} \sum_{m=1}^3 \bar{\phi}^m \epsilon_{jk} \Delta x_k^m \right) \quad (8)$$

Therefore, the flow into the node 1 is:

$$Q_{\Delta 123 \rightarrow 1} = -\frac{q_i n_i^{(1)} L^{(1)}}{2} \quad (9)$$

where $n_i^{(1)}$ and $L^{(1)}$ are the external normal unit vector and length of the edge opposite to pore node 1 in the triangular element.

The flow into pore node 2 $Q_{\Delta 123 \rightarrow 1}$ from the triangular element $\Delta 231$ can be obtained in this way. The flow into pore node 1 from other triangular elements that directly connect to the pore node can be obtained. In this way, the total flow into pore node 1 can be expressed as:

$$Q_{\text{total}} = Q_{\Delta 123 \rightarrow 1} + Q_{\Delta 137 \rightarrow 1} \quad (10)$$

According to Eq. (6), the pore pressure at pore node 1 is updated by:

$$p_{t+\Delta t}^p = p_t^p + \frac{M(Q_{\text{total}} - \Delta V_{\text{mech}})}{V} \Delta t \quad (11)$$

where M is the Biot modulus, if the Biot coefficient α is equal 1, $M = \frac{K_w}{n}$. Otherwise, $M = \frac{K_w}{n + (\alpha - n)(1 - \alpha) \frac{K_w}{K}}$, where K is the drained bulk modulus of the porous medium, K_w is the fluid bulk modulus, α is the Biot coefficient, n is porosity. Please see references [20, 77].

The time step must be less than the critical time to ensure the stability of the numerical calculation. The critical time step is given by:

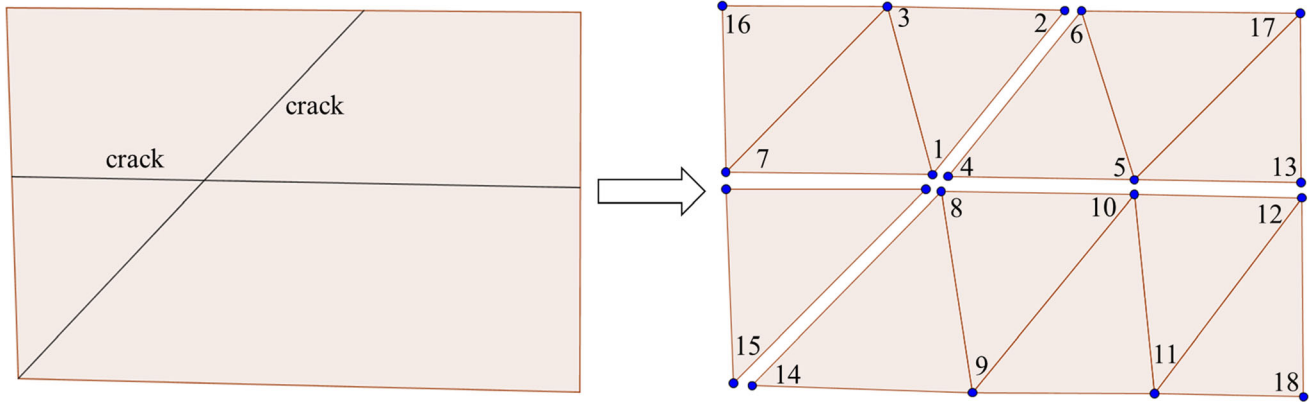


Fig. 2 Pore seepage model for fractured rock mass

$$\Delta t_f = \min \left[\frac{V}{M \sum_i \rho_w g k_i} \right] \tag{12}$$

where k_i is the isotropic permeability coefficient.

2.3 Fluid exchange at the fracture

In Fig. 3, assume the fracture pressure at fracture nodes $c1$ and $c2$ is p_{c1}, p_{c2} , and the pore pressures at pore nodes 1, 7, and 0, 16 on both sides of the fracture are p_1, p_7 and p_0, p_{16} , respectively. The length of the fracture is L and h is the

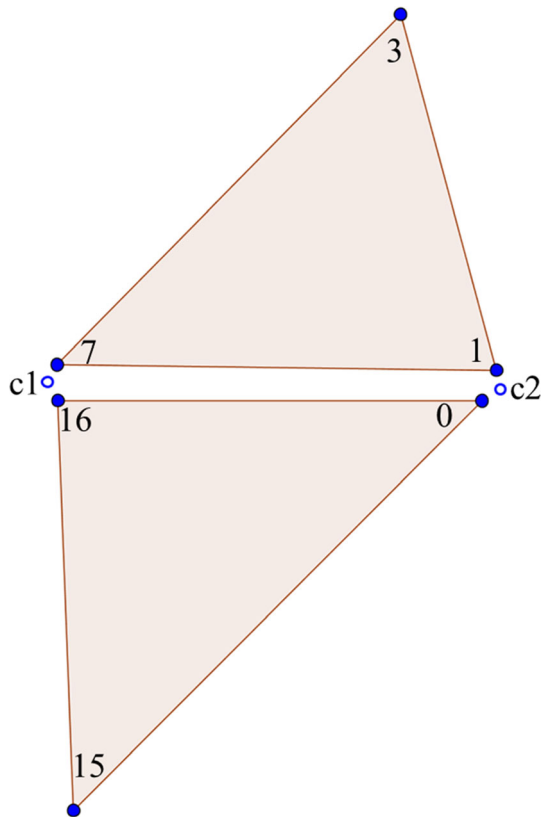


Fig. 3 Pore seepage-fracture seepage coupling treatment

exchange coefficient of the fluid at the fracture. Therefore, the fluid exchange per unit time between the fracture $c1c2$ and the edge 17 is:

$$\begin{aligned} Q_e &= h \left(\frac{(p_{c1} + p_{c2})}{2} - \frac{(p_1 + p_7)}{2} \right) L \\ &= h \frac{(p_{c1} - p_{c7})}{2} L + h \frac{(p_{c2} - p_1)}{2} L \end{aligned} \tag{13}$$

Therefore, the fluid exchange per unit time at fracture $c1c2$ is distributed to pore node 1 as follows:

$$Q_{c1c2 \rightarrow 1} = h \frac{(p_{c2} - p_1)}{2} L_{17} \tag{14}$$

Similarly, the fluid exchange per unit time at fracture $c2c3$ is distributed to pore node 1 as follows:

$$Q_{c2c3 \rightarrow 1} = h \frac{(p_{c2} - p_1)}{2} L_{12} \tag{15}$$

Therefore, the pore pressure of pore node 1 located in the fracture is finally updated by:

$$P_{t+\Delta t}^p = P_t^p + \frac{M(Q_{total} + Q_{c1c2 \rightarrow 1} + Q_{c2c3 \rightarrow 1} - \alpha \Delta V_{mech})}{V} \Delta t \tag{16}$$

For the fracture node $c2$, the pore nodes 0, 1, 4, and 8 all exchange fluid with it. Therefore, the total fluid exchange between the fracture node $c2$ and the porous medium is:

$$\begin{aligned} Q_e &= h \frac{(p_{016} - p_{c2})}{2} L_{016} + h \frac{(p_1 - p_{c2})}{2} L_{17} \\ &\quad + h \frac{(p_1 - p_{c2})}{2} L_{12} + h \frac{(p_4 - p_{c2})}{2} L_{46} \\ &\quad + h \frac{(p_4 - p_{c2})}{2} L_{45} + h \frac{(p_8 - p_{c2})}{2} L_{810} \end{aligned} \tag{17}$$

Therefore, the pore pressure at the fracture node $c1$ is finally updated by:

$$p_{t+\Delta t}^f = p_t^f + K_w(Q_c + Q_e) \frac{\Delta t}{V} - K_w \frac{\Delta V}{V_m} \tag{18}$$

2.4 The effect of fracture extension on the fracture seepage and pore seepage

Existing fractures may extend or new fractures may be generated. The node sharing relationship of adjacent triangular elements at the fractures should be updated. The flow calculation of these nodes at the newly generated fractures also changes. As shown in Fig. 4, the original adjacent triangular element 137 and triangular element 123 are separated, and a new fracture $c2c7$ is generated. Pore node 3 is separated into two pore nodes 3 and 3', and pore node 1 is separated into two pore nodes 1 and 1'.

The effect of fracture propagation on the calculation of fracture seepage is shown in Fig. 4. The fracture node $c2$ is still taken as an example. The flow rate at this fracture node needs to add $q_{c7 \rightarrow c1}$, $Q_{L13 \rightarrow c2} = h \frac{(p_1 - p_{c2})}{2} L_{13}$, and $Q_{L1'3' \rightarrow c2} = h \frac{(p_{1'} - p_{c2})}{2} L_{1'3'}$ to the original Eq. (14), where

$$q_{c7 \rightarrow c2} = \frac{1}{12\mu} a^3 \frac{\Delta p}{L} \tag{19}$$

The triangular element $\Delta 123$ and $\Delta 137$ in Fig. 3 are separated. Therefore, from the triangular element $\Delta 1'23'$, no longer flows directly into pore node 1 but from a newly

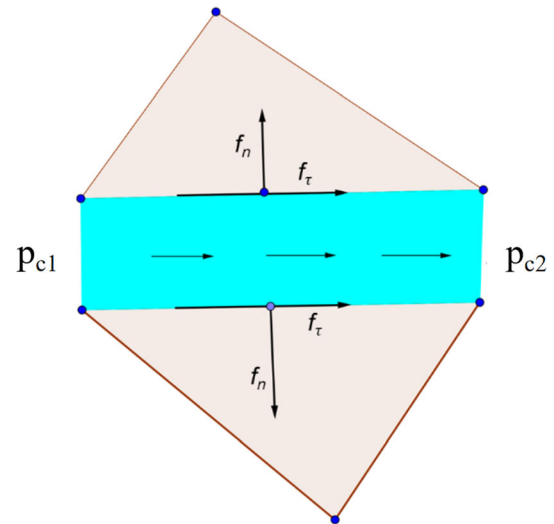


Fig. 5 Fluid flow and force in the fracture

generated fracture $c2c7$ into node 1. That is why it is necessary to replace $Q_{\Delta 123 \rightarrow 1}$ with $Q_{c2c7 \rightarrow 1}$ in Eq. (10), where

$$Q_{c2c7 \rightarrow 1} = h \frac{(p_{c2} - p_1)}{2} L_{13} \tag{20}$$

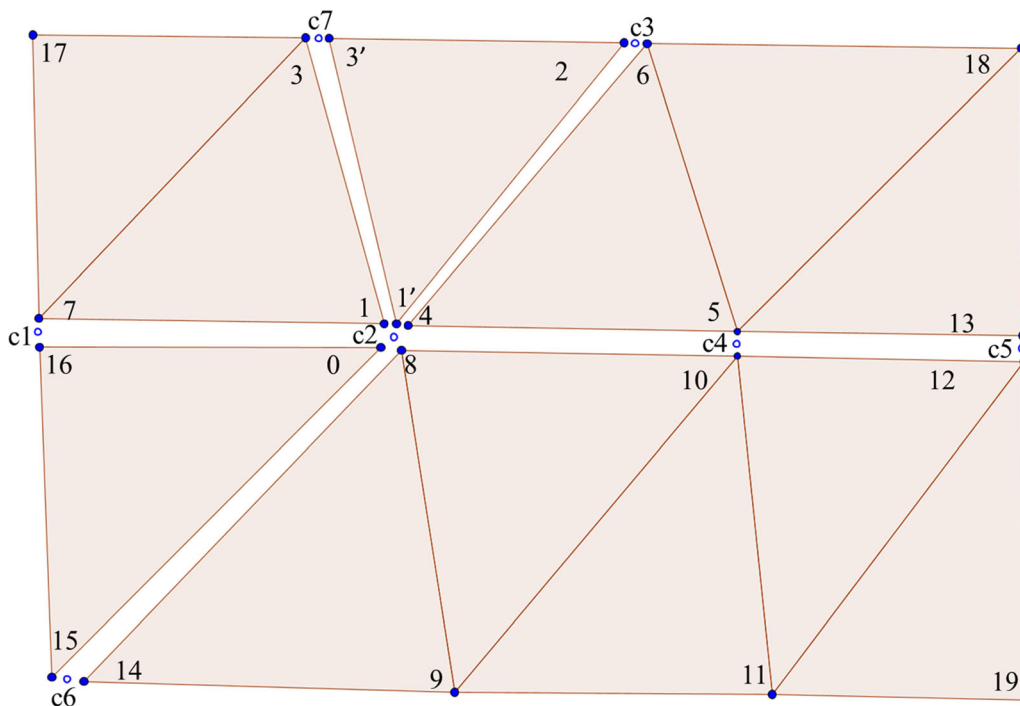


Fig. 4 The influence of fracture propagation on seepage calculation

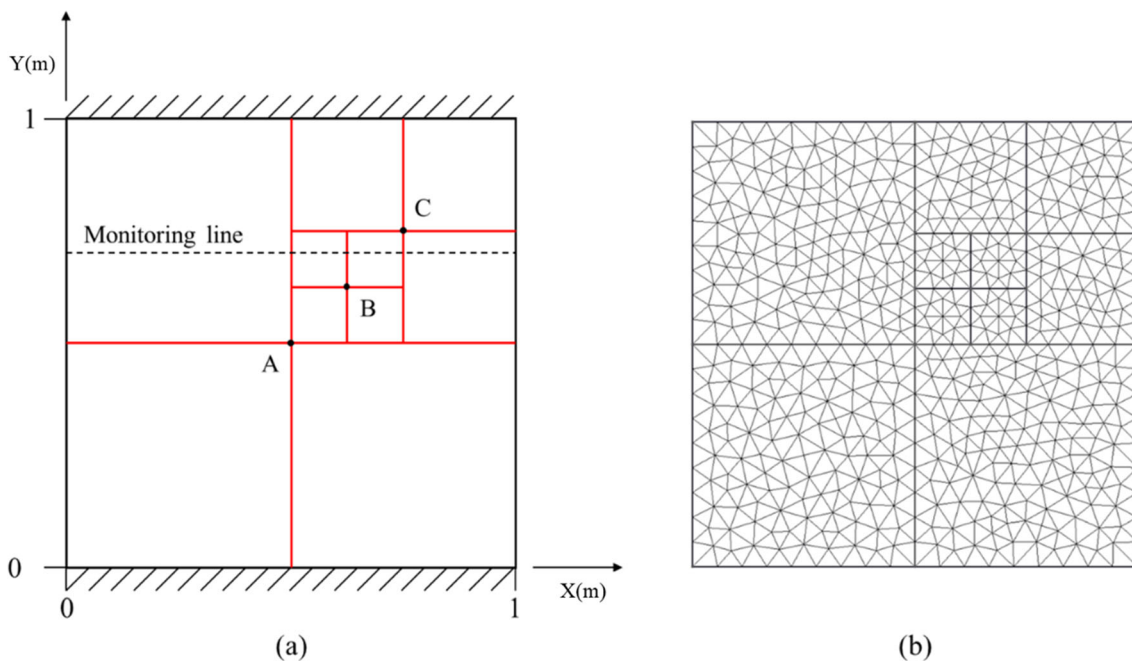


Fig. 6 Geometric model and computational mesh

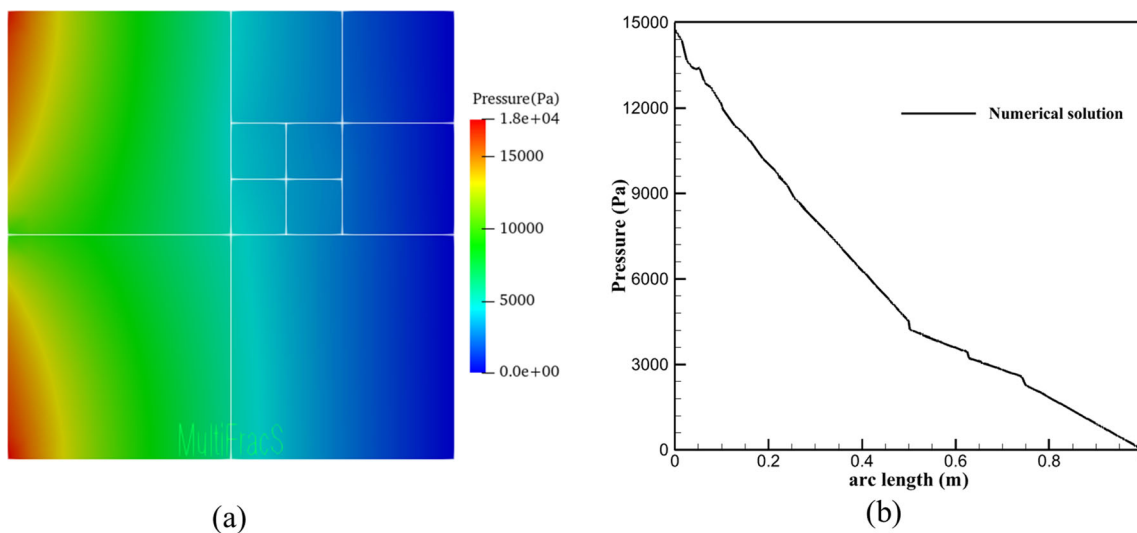


Fig. 7 Pore pressure distribution obtained by the 2D continuous-discrete mixed seepage model: **a** pore pressure distribution, **b** pore pressure distribution at the monitoring line $y = 0.7$

3 Hydro-mechanical coupling model

3.1 The basic idea of hydro-mechanical coupling

The mixed seepage model can be combined with FEM, DEM, FDEM, DDA, NMM, and other numerical methods to construct appropriate hydro-mechanical coupling models. The general framework for constructing the hydro-mechanical coupling model is given here, i.e., the hydro-mechanical coupling model includes the following processes: (1) Fluid flowing in a fracture exerts a

corresponding fracture pressure on the fracture. Under the action of the fracture pressure, the fracture may close or open. According to the cubic law, the opening or closing of the fracture affects the flow rate of the fluid in the fracture and thus, changes the fracture pressure; (2) The pore seepage in the matrix exerts pore pressure. The volume of the pores changes under stress, which changes the permeability of the matrix. The change in permeability of the matrix, in turn, affects the flow rate and pore pressure of the fluid in the matrix.

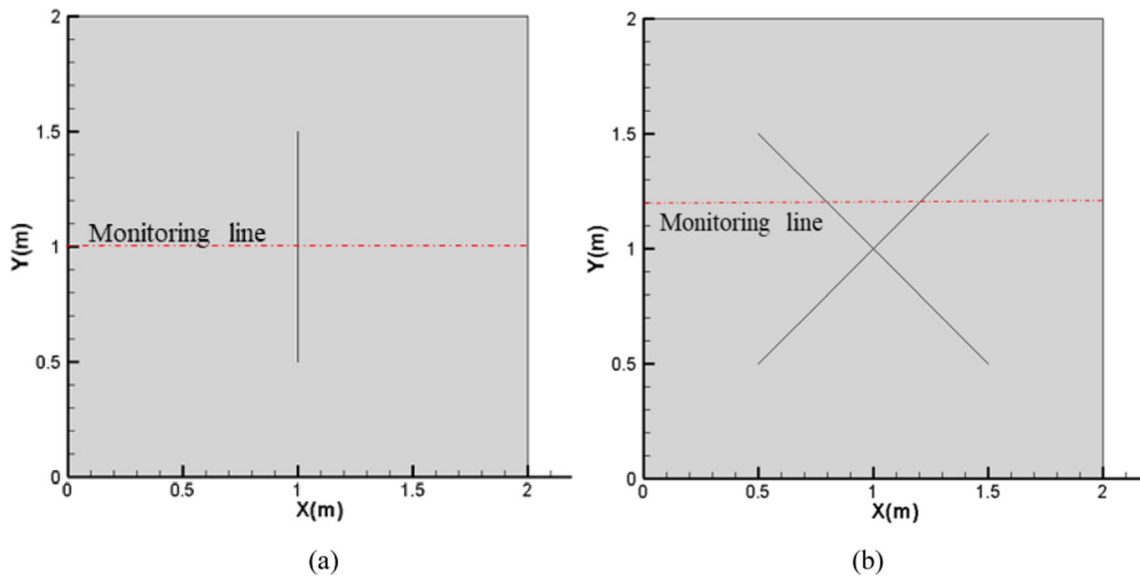


Fig. 8 Model geometric conditions and monitoring line settings

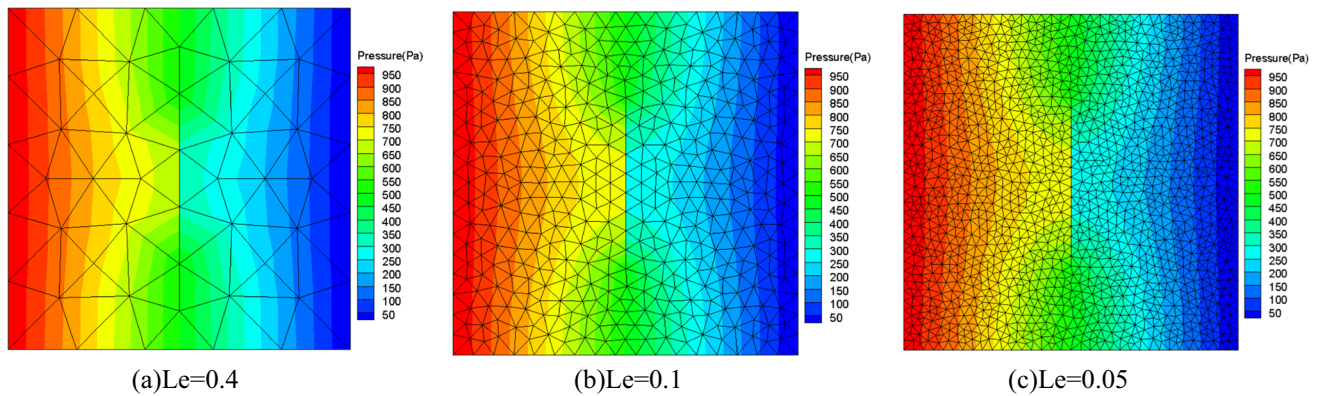


Fig. 9 Pore pressure distribution under different element sizes

Taking FDEM as an example, a hydro-mechanical coupling model is constructed based on the 2D continuous-discrete mixed seepage model. First, we briefly introduce the basic principles of FDEM.

3.2 Basic principles of FDEM

In 2D FDEM, the continuum is discretized into a finite element mesh of triangular elements. A four-node cohesive joint element is added on the common edge of adjacent triangular elements, as shown in Fig. 1. FDEM uses the finite element method to solve the stress and strain of the constant strain triangular elements and uses the discrete element method to deal with the contact between the triangular elements. In addition, the breaking of the joint element characterizes the fracture and fragmentation of the continuum. Please refer to the literature for potential

contact force, the governing equation, contact detection, and fracture criterion of joint elements in FDEM [52].

3.2.1 Deformation of solid medium

In FDEM, the solid domain of interest is meshed into a series of triangular solid elements. The deformation and stress of a single solid element are calculated by a large strain displacement formulation for the finite element side of FDEM. Recently, this formulation has been generalized through the so-called Munjiza material element concept. For homogeneous and isotropic materials, the constitutive relation is given by

$$\mathbf{T} = \frac{1}{\sqrt{|\det \mathbf{F}|}} \left[\frac{E}{1 + \nu} \mathbf{E}_d + \frac{E}{1 + \nu} \mathbf{E}_s + 2\mu \mathbf{D} \right] \tag{21}$$

where T is the stress tensor in the overall coordinate after element deformation; F is the deformation gradient; E_d and

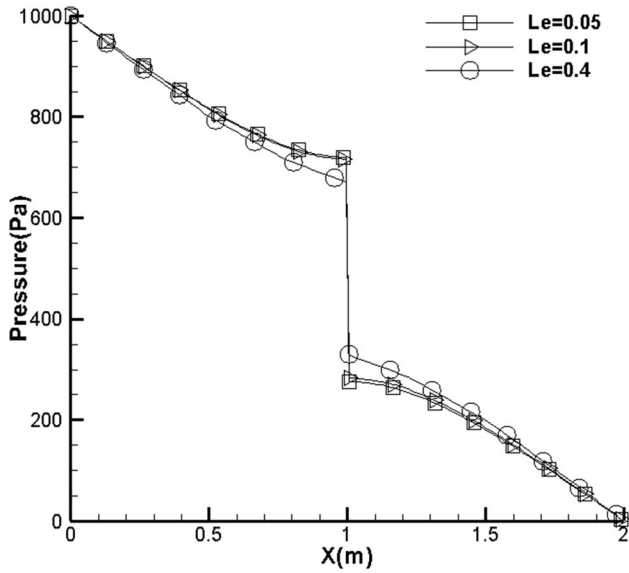


Fig. 10 The pore pressure distribution at the monitoring line $y = 1$ under different element sizes

E_s are Green and St. Venant strain tensors due to the shape and volume change, respectively; E and ν are Young’s modulus and Poisson’s ratio, respectively; μ is viscous damping coefficient, and D is the strain rate tensor. As triangular solid elements in FDEM yield constant strains, the equivalent nodal force of each edge caused by the deformation of triangular elements can be calculated by

$$\mathbf{f}_n = \frac{1}{2} \mathbf{T} \mathbf{n} = \frac{1}{2} \begin{bmatrix} \sigma_{xx} & \sigma_{xy} \\ \sigma_{yx} & \sigma_{yy} \end{bmatrix} \begin{bmatrix} n_x \\ n_y \end{bmatrix} \quad (22)$$

where n is the outward normal vector of the triangular element edge.

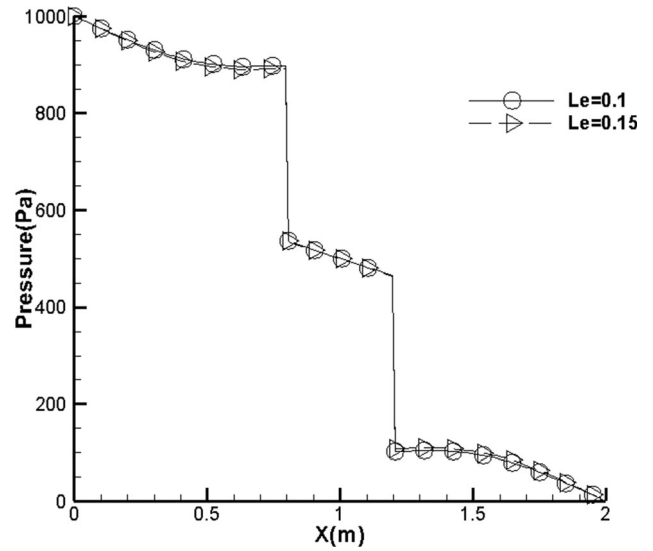


Fig. 12 The pore pressure distribution along the monitoring line $y = 1.2$ m under different element sizes

3.3 The influence of fluid on solids

3.3.1 The effect of fracture seepage on solid

As shown in Fig. 5, suppose the fracture pressure at fracture nodes 1 and 2 are p_{c1} and p_{c2} , respectively. Then, the total normal force acting on two walls of the fracture is:

$$f_n = \frac{(p_{c1} + p_{c2})}{2} L_{c1c2} \quad (23)$$

The two walls of the fracture are subjected to a tangential viscous force exerted by the fluid. The total tangential force acting on the fracture walls is

$$f_\tau = L_{c1c2} \tau_{f0} = \frac{a}{2} \Delta P \quad (24)$$

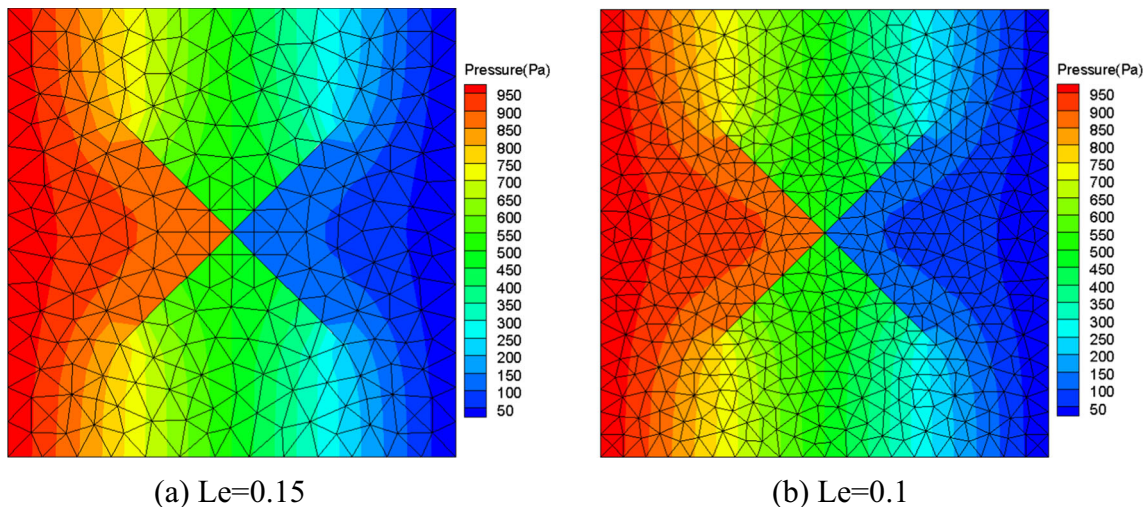


Fig. 11 Pore pressure distribution under different element sizes

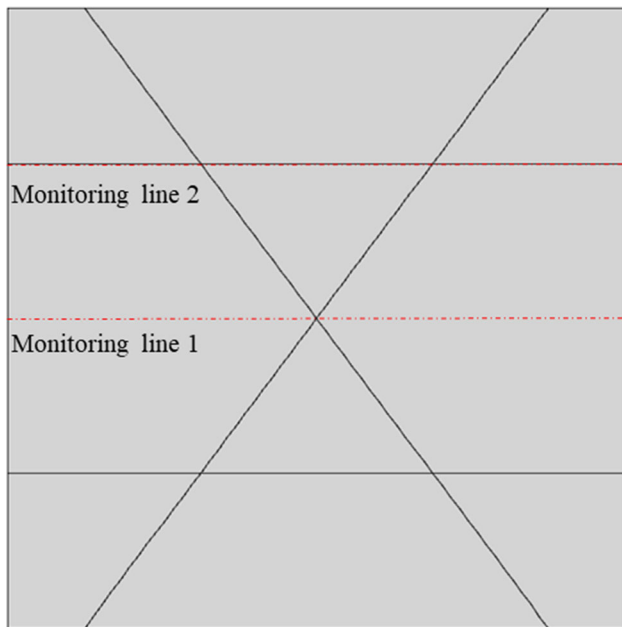


Fig. 13 Model geometry conditions

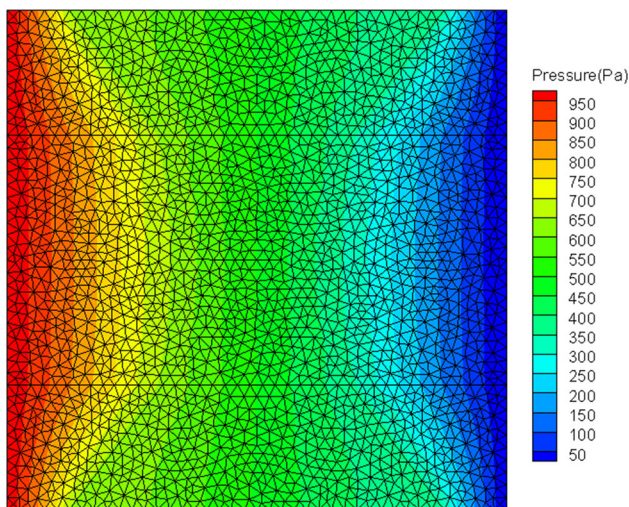


Fig. 14 Results of water pressure distribution

where L_c is the length of the fracture.

In this way, the fracture fluid pressure and viscous force can be obtained by introducing the fluid flow algorithm mentioned above.

3.3.2 The influence of pore seepage on solid

The effective stress in the rock matrix can be expressed as:

$$\sigma'_{ij} = \sigma_{ij} - \alpha p \delta_{ij} \tag{25}$$

where α is the Biot coefficient.

Thus, the stress increment induced by the pore pressure is:

$$\Delta\sigma_{ij} = -\alpha p \delta_{ij} \tag{26}$$

We apply the stress increment as a body load to the triangular element.

3.4 The effect of solid on fluid

3.4.1 The influence of solid deformation and fracturing on fracture seepage

The aperture of the fracture is affected by the change of solid deformation effects and thus, changes the permeability of the fracture. According to Eq. (4), the intrinsic permeability of the fracture becomes $k = k_0(a/a_i)^2$ when the aperture of the fracture changes, where k_0 is the intrinsic permeability of the fracture at the initial moment, a_i is the hydraulic aperture of the fracture at the initial moment and a is the hydraulic aperture at the current moment.

The flow network of fracture seepage is altered by solid fracturing. Fracture pressure and flow rate are also altered. Combined with the fracturing of the joint element and Eq. (4), these changes will be automatically handled in the hydro-mechanical coupling model. In conventional seepage-stress coupling models, the effect of fracturing on the seepage in the fracture cannot be considered.

3.4.2 The influence of solid deformation and fracturing on pore seepage

The following coupling equation expresses the influence of solid deformation on pore seepage:

$$k_{ij}(\sigma, p) = k_0 e^{-\beta \left(\frac{\sigma_{ii}/3 - p}{H} \right)} \tag{27}$$

$$\sigma_{ii} = \sigma_{11} + \sigma_{22} + \sigma_{33}$$

where β is the coupling parameter, H is Biot constant, and $\sigma_{ii}/3$ is the average total stress, representing the degree of influence of stress–strain on permeability coefficient. The smaller is the β , the smaller the influence of stress on matrix permeability, and its value is determined by the experiment.

The fracturing effect on pore seepage is automatically considered by updating the pore node shared relationship of triangular elements across the fracture.

4 Examples

4.1 Single fracture-pore mixed seepage

We use the 2D mixed seepage model in this paper to calculate a porous media with multiple horizontal and vertical

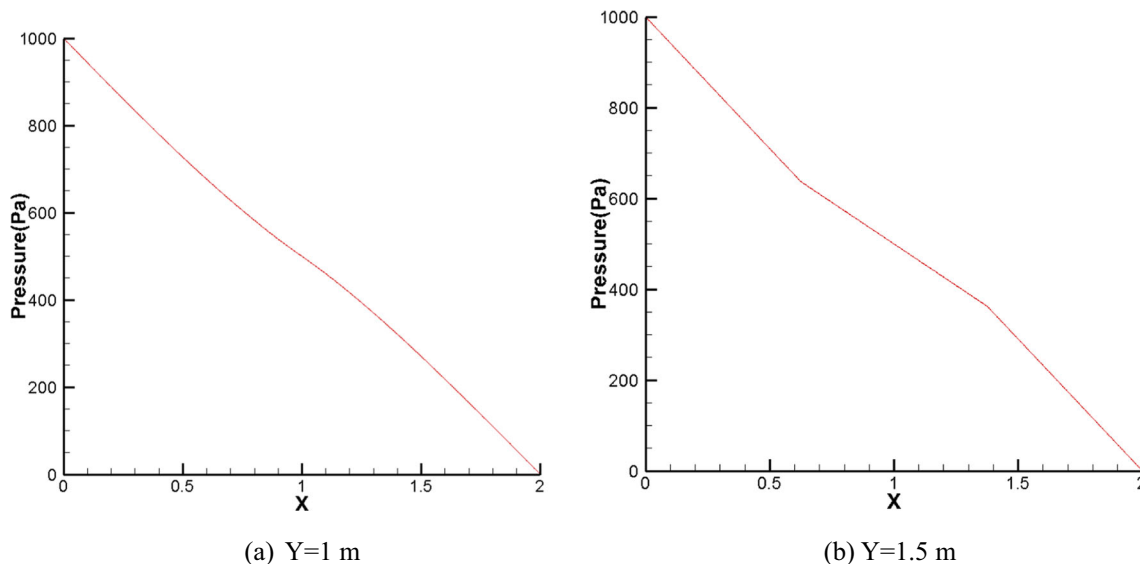


Fig. 15 Water pressure distribution along the monitoring line

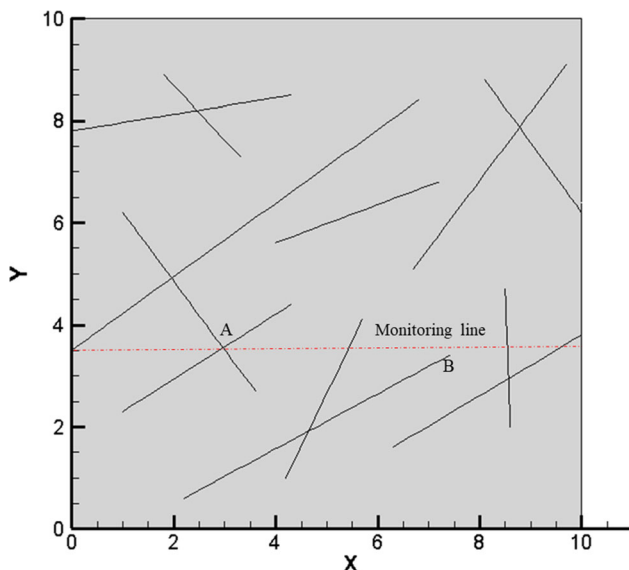


Fig. 16 Model geometry conditions

fractures [12], as shown in Fig. 6. The coordinates of points A, B, and C are (0.5, 0.5), (0.625, 0.625), and (0.75, 0.75), respectively. A constant injection flow rate of $1\text{ m}^3/\text{s}$ is applied on the model’s left side, and the pore pressure on the right side is 0 Pa. The intrinsic permeability of the model is $1 \times 10^{-7} \text{ m}^2$, fluid viscosity coefficient $\mu=0.001 \text{ Pa} \cdot \text{s}$. The aperture of the fracture is 0.00865.

The numerical solution obtained by the 2D continuous-discrete mixed seepage model is shown in Fig. 7. The distribution of pore pressure exhibits a trend similar to the literature results [12].

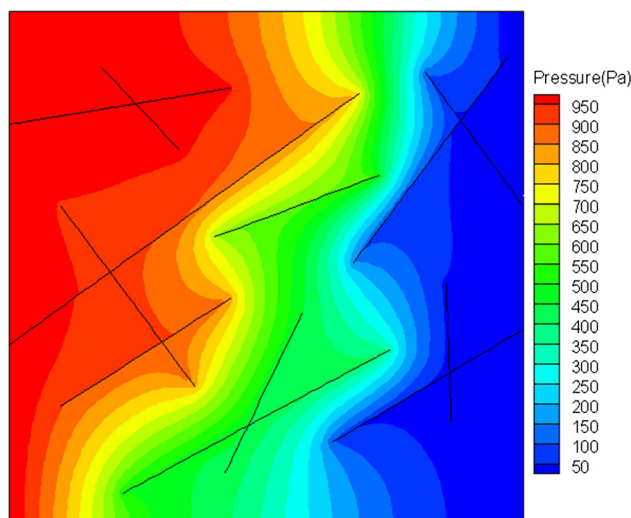


Fig. 17 Water pressure distribution results

4.2 The seepage problem of porous media with impervious fractures

We use the 2D continuous-discrete mixed seepage model to study the effects of impermeable fractures on pore seepage. As shown in Fig. 8, both computational models have $2 \text{ m} \times 2 \text{ m}$ square areas and the pore pressure at the left boundary is fixed at 1000 Pa. The pore pressure at the right boundary is fixed at 0 Pa, and the other boundaries are impermeable. In model 1, there is only one vertical fracture, while in model 2, there are two diagonal fractures perpendicular to each other. The intrinsic permeability of the model is $1 \times 10^{-12} \text{ m}^2$, fluid viscosity coefficient $\mu=0.001 \text{ Pa} \cdot \text{s}$.

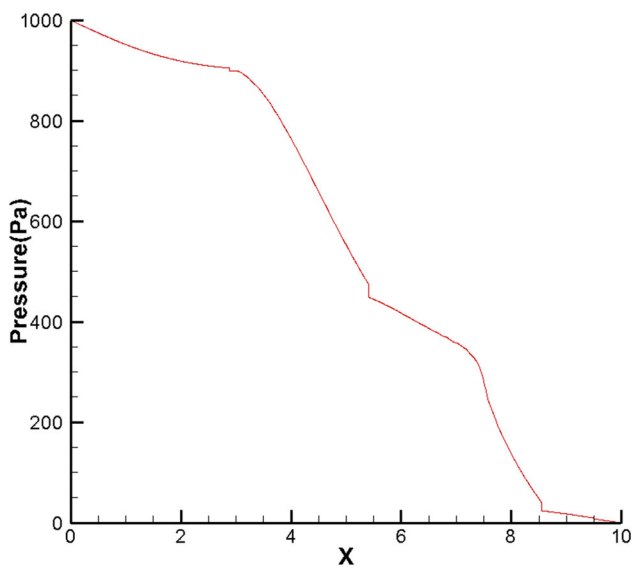


Fig. 18 Water pressure distribution along the monitoring line

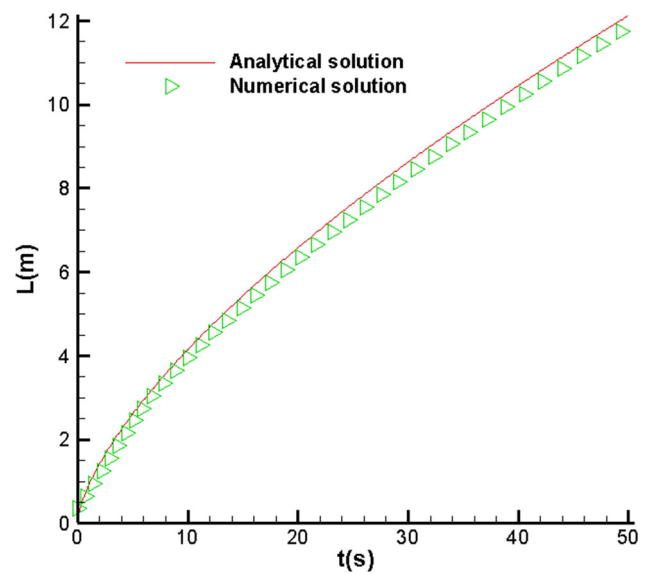


Fig. 20 Evolution of fracture length with time

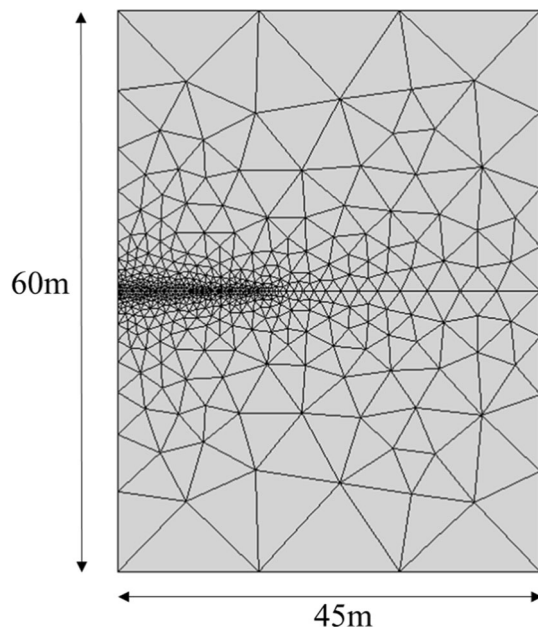


Fig. 19 Computational mesh for KGD model

For model 1, we used three different mesh sizes for the simulation. The sizes of the smallest element $L_e = 0.4, 0.1, 0.05$ m, and the simulation results are shown in Fig. 9. In addition, there is a monitoring line at $y = 1$. The pore pressure distribution along the monitoring line is shown in Fig. 10. For $L_e = 0.1$ and 0.05 m, the pore pressure distribution along the monitoring line is essentially the same. While for $L_e = 0.4$ m, the pore pressure has a large deviation compared with that of $L_e = 0.1$ or 0.05 m; because of the large size of the element, the calculation accuracy is insufficient. Nevertheless, for the three mesh sizes, all the

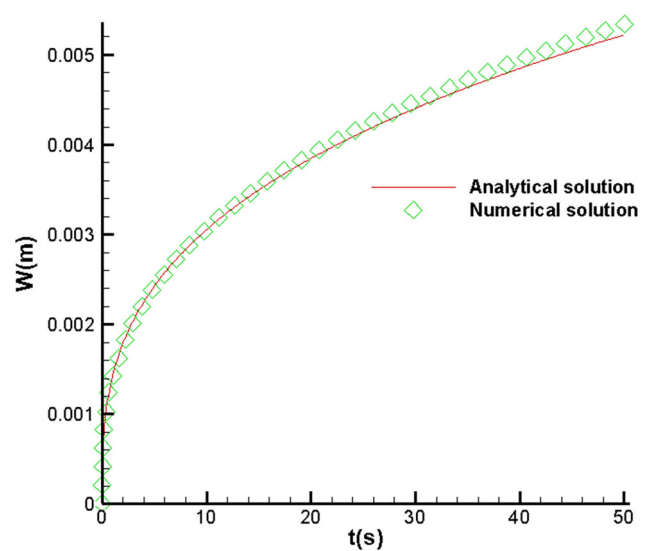


Fig. 21 Evolution of fracture width over time

pore pressure distribution and the monitoring line jump at the fracture.

For model 2, we use $L_e = 0.15$ and 0.1 m to discretize the domain. The simulation results are shown in Fig. 11. The pore pressure distribution along the monitoring line $y = 1.2$ m is shown in Fig. 12. The results of the two element sizes are in good agreement. The pore pressure along the monitoring line also jumps at the intersection of the monitoring line and the two fractures.

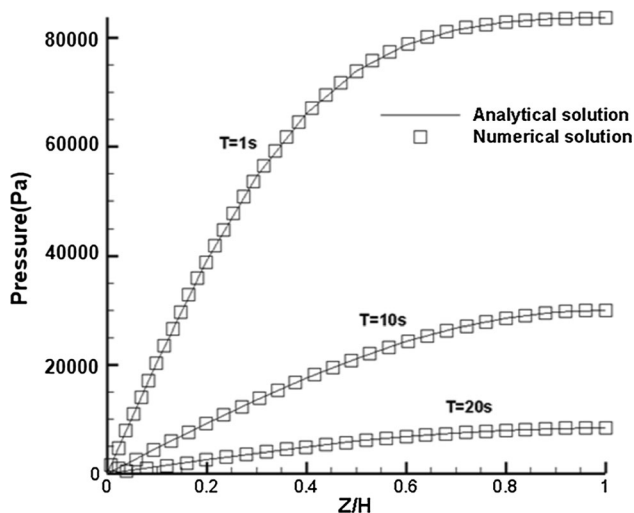


Fig. 22 The distribution of soil pore pressure along with the height at different times

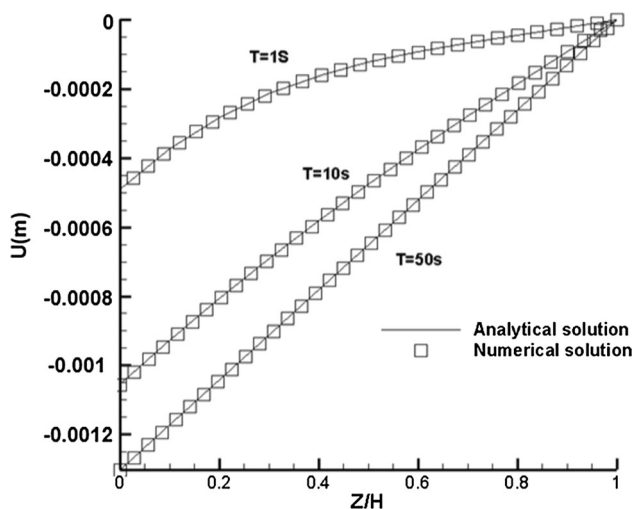


Fig. 23 The soil displacement distribution along with the height distribution at different times

4.3 Mixed seepage problem for porous media with permeable fracture

4.3.1 Multi-fractures-pore mixed seepage

This section uses the 2D continuous-discrete seepage model to calculate an example with two sets of inclined and horizontal permeable fractures. Fluids flow not only in the rock matrix but also in the fractures. In Fig. 13, the pore pressure setting is the same as in the calculation example in 4.2.

Figure 14 shows the result of the water pressure distribution. From the water pressure distribution at $y = 1.5$ shown in Fig. 15, it is evident that there are obvious inflection points of the water pressure at the intersections of the fractures. In contrast, the water pressure is linearly distributed in other areas. This reflects the influence of the seepage water from the fractures on the pore pressure.

4.3.2 Arbitrarily complex fracture-pore mixed seepage

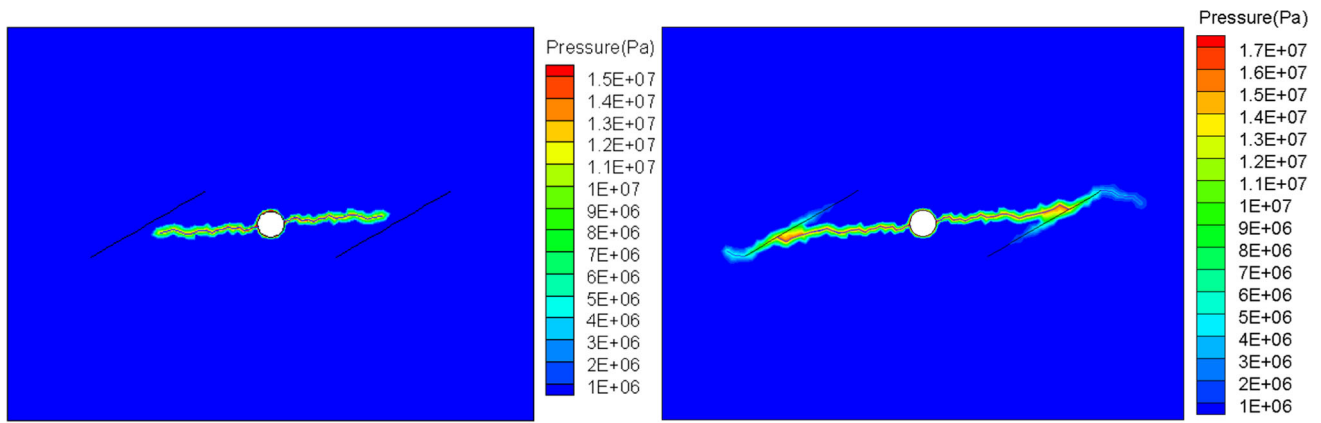
We use the 2D continuous-discrete mixed seepage model to solve the complex problem of mixed seepage from fractures and pores. A rectangular area of 10×10 m contains 12 intersecting fractures, as shown in Fig. 16. The pore pressure setting is the same as in the calculation example in 4.2.

The simulation results are shown in Fig. 17. The water pressure displays a step-like distribution, reflecting well the influence of fracture seepage on the pore pressure. The monitoring line at $Y = 3.5$ m, and the pore water pressure distribution along the monitoring line are shown in Fig. 18. Initially, the pore pressure dropped slowly along the monitoring line. When passing through point A at the intersection of two fractures, the pore pressure is significantly reduced, reflecting the preferential diversion effect of the fractures. The pore water pressure also suddenly decreases when the next fracture endpoint B is given.

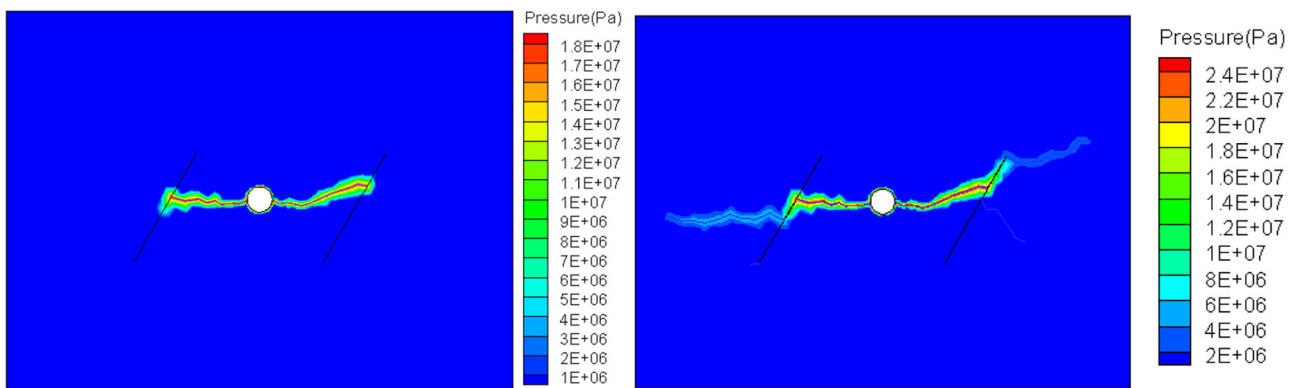
4.4 Hydro-mechanical coupling problem

4.4.1 Fracture seepage-stress coupling (KGD)

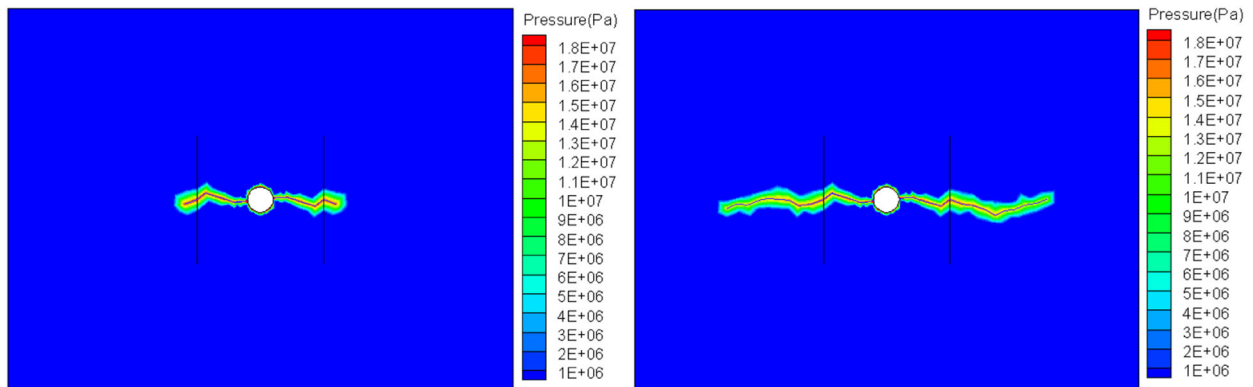
In this section, the KGD model is employed to verify the hydro-mechanical coupling model. As shown in Fig. 19, the model is a rectangle of $45 \text{ m} \times 60 \text{ m}$. The left and right boundaries are fixed along the x -direction, and the upper and lower boundaries are fixed along the y -direction. The injection point is set to the origin of the x -axis. The injection flow rate Q is a constant $0.001 \text{ m}^2/\text{s}$, and the four boundaries are impervious. The fluid density $\rho = 1000 \text{ kg/m}^3$, fluid viscosity coefficient $\mu = 0.001 \text{ Pa} \cdot \text{s}$, the solid elastic modulus E is 17 GPa , and Poisson's ratio ν is 0.2 . This example does not consider the in situ stress and fluid loss in the fracture. The analytical solution to this problem is as follows [9]:



(a) 30° Dilated (Modeling)



(b) 60° Arrested (Modeling)



(c) 90° Crossed (Modeling)

Fig. 24 The influence of discrete fracture on hydraulic fracture propagation under different natural fracture inclination angles

$$L = 0.48 \left(\frac{4E'Q^3}{\mu} \right)^{\frac{1}{6}} t^{\frac{2}{3}} \tag{28}$$

$$W = 1.32 \left(\frac{16\mu Q^3}{E'} \right)^{\frac{1}{6}} t^{\frac{1}{3}} \tag{29}$$

where E' is the elastic modulus of plane strain, $E' = \frac{E}{1-\nu^2}$, Q is the injected flow.

The numerical solutions obtained by the hydro-mechanical model are shown in Figs. 20 and 21. In the present paper, the numerical solutions are in good agreement with

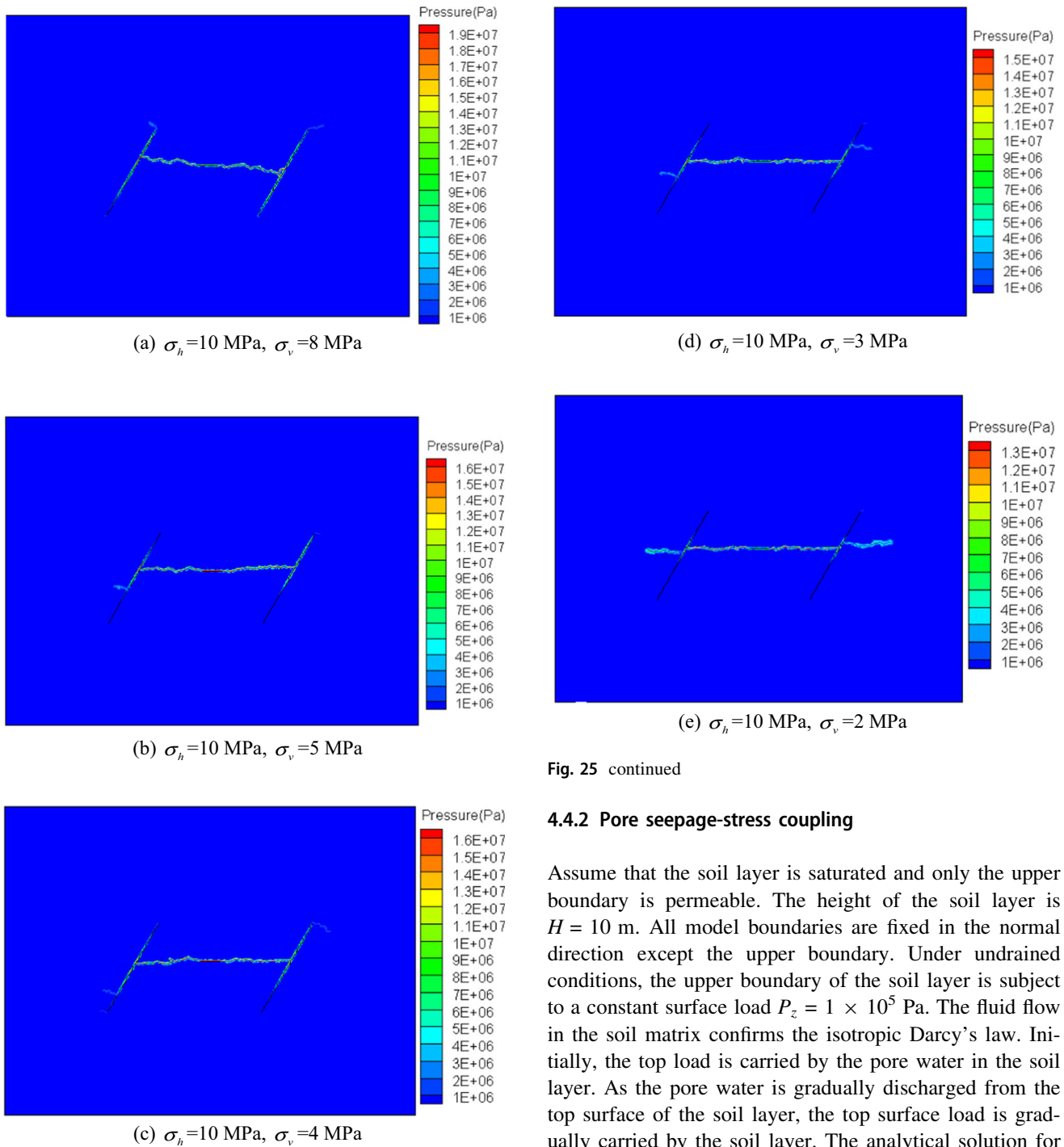


Fig. 25 continued

4.4.2 Pore seepage-stress coupling

Assume that the soil layer is saturated and only the upper boundary is permeable. The height of the soil layer is $H = 10$ m. All model boundaries are fixed in the normal direction except the upper boundary. Under undrained conditions, the upper boundary of the soil layer is subject to a constant surface load $P_z = 1 \times 10^5$ Pa. The fluid flow in the soil matrix confirms the isotropic Darcy’s law. Initially, the top load is carried by the pore water in the soil layer. As the pore water is gradually discharged from the top surface of the soil layer, the top surface load is gradually carried by the soil layer. The analytical solution for one-dimensional consolidation of pore pressure and displacement is as follows [10]:

$$P = 2P_0 \sum_{m=0}^{\infty} \frac{\sin(a_m \hat{z})}{a_m} e^{-a_m^2 \hat{t}} \tag{30}$$

$$u_z = \frac{HP_z}{\alpha_1} \left(2\alpha \frac{P_0}{P_z} \left[\sum_{m=0}^{\infty} \frac{\cos(a_m \hat{z})}{a_m^2} e^{-a_m^2 \hat{t}} \right] + \frac{\hat{z}}{z} - 1 \right) \tag{31}$$

Fig. 25 The influence of in situ stress on the interaction of two kinds of fractures

the analytical solutions, which verifies the correctness of the hydro-mechanical coupling model.

where $P_0 = \frac{\alpha}{\alpha_1} P_z$, $a_m = \frac{\pi}{2}(2m + 1)$, $\hat{Z} = \frac{H-z}{H}$, $\hat{t} = \frac{ct}{H^2}$, $c = \frac{k}{\mu S}$, $S = \frac{1}{M} + \frac{\alpha^2}{\alpha_1}$ is the storage water coefficient, α is the Biot coefficient, M is the Biot modulus.

The calculation parameters are as follows: shear modulus $G = 2 \times 10^8$ Pa, the drainage bulk modulus $K = 5 \times 10^8$ Pa, Biot modulus $M = 4 \times 10^9$ Pa, Biot coefficient $\alpha = 1$, intrinsic permeability $k = 8 \times 10^{-12}$ m², fluid density $\rho = 1000$ kg/m³, fluid viscosity coefficient $\mu = 0.001$ Pa. Figures 22 and 23 show the distribution of pore pressure and displacement along with the height at different times. The numerical solution is in good agreement with the analytical solution, which verifies the correctness of the hydro-mechanical coupling model to deal with the pore seepage-stress coupling problem.

4.5 Application examples of hydraulic fracturing

In this section, we investigate the interaction between discrete fracture and hydraulic fractures. The effect of the angle of approach and in situ stress on fracture propagation is analyzed. The size of the model is 0.8 m \times 0.6 m, and the inclination angles of the two parallel fractures are 30°, 60°, and 90°. The horizontal and vertical in situ stresses are set to $\sigma_h = 8$ MPa and $\sigma_v = 3$ MPa, respectively. The viscosity of fracturing fluid is 1.0×10^{-3} Pa, and the injection flow rate is 8.5×10^{-4} m³/s. We compared the simulated interaction mode of hydraulic and discrete fracture with Zhou et al. [79]. Three basic interaction models of hydraulic and discrete fracture, namely, Dilated, Arrested, and Crossed, are reproduced.

Hydraulic fractures initiate and extend along the direction of vertical minimum in situ stress when the natural fracture angle is 30° as shown in Fig. 24a. As two types of fractures meet, hydraulic fracture enters the natural fracture. The natural fracture away from the injection hole starts to initiate and continues to extend in the vertical minimum in situ stress direction. Hydraulic fractures initiate and extend along the direction of vertical minimum in situ stress when the natural fracture angle is 60° as shown in Fig. 24b. After the two types of fractures intersect, it enters the natural fracture. Then, it re-opens from a point with a certain distance from the intersection point and continues to extend in the direction of the maximum in situ stress. As shown in Fig. 24c, when the natural fracture angle is 90°, the hydraulic fracture starts and extends along the direction of vertical minimum in situ stress. When encountering discrete fracture, it continues to extend directly through the discrete fracture.

Next, we discuss the influence of in situ stress on the interaction between hydraulic fractures and discrete fracture. In the simulation, we choose a model with a natural fissure angle of 60° for the analysis. The horizontal in situ

stress is constant at 10 MPa, and the vertical in situ stress varies between 2 and 8 MPa. Other parameters remain unchanged. The simulation results are shown in Fig. 25. The simulation results show that the hydraulic fractures all propagate in the direction of maximum in situ stress before intersecting with discrete fracture. After the hydraulic fracture intersects with the natural fracture, the hydraulic fracture enters the natural fracture. The hydraulic fractures reopen and extend in the direction of maximum in situ stress after some deviation from the intersection. As the difference in in situ stress increases, the offset distance of hydraulic fractures gradually decreases, which is more conducive for hydraulic fractures to pass directly through the discrete fracture. This simulation phenomenon is consistent with Zhou et al. [79].

5 Discussion

The advantage of the 2D continuous-discrete mixed seepage model is that a pore-fracture seepage boundary describes the fluid exchange between the fluid in the fracture and the rock matrix. Unlike in the literature [52, 59], the discontinuity of pore pressure across fractures is well solved in this model. Moreover, the fluid exchange in the 2D continuous-discrete mixed seepage model is determined only based on the difference between fracture and pore pressure, without artificially assuming that the fracture pressure is equal to the pore pressure on both sides of the fracture.

The continuous-discrete seepage model considers the influence of fracture generation and extension on the pore seepage. Once the fracture is generated and extended, the node sharing relationship of adjacent triangular elements on both sides of the fracture is dynamically updated for pore seepage calculation. The adjacent triangular elements on both sides of the fracture will no longer share the pore pressure node, so the pore pressures on both sides may not be equal. Therefore, the effect of the fracture initiation and propagation of the fracture on the pore seepage can be well considered. However, in the literature model [52, 59], the media on both sides still share pore pressure nodes even after cracks are generated.

6 Conclusion

A 2D continuous-discrete mixed seepage model that considers the fluid exchange and the pore pressure discontinuity at the fracture is presented. In this model, the joint element and its large exchange coefficients do not need to introduce for the pore seepage calculation. Therefore, the computational efficiency is greatly improved compared to

the model in the literature [62]. Subsequently, the continuous-discrete mixed seepage model is combined with FDEM to build a 2D hydro-mechanical coupling model to simulate the initiation, extension, intersection, and interaction of fractures driven by fluid, as well as the evolution of fluid pressure in fractures and rock matrix.

Acknowledgements This work was supported by the GHfund A (20220201, ghfund20202019662).

Data availability All data generated or analyzed during this study are included in this published article.

References

- Abe H, Keer L, Mura T (1976) Growth rate of a penny-shaped crack in hydraulic fracturing of rocks. *J Geophys Res* 81(35):6292–6298
- AbuAisha M, Eaton D, Priest J, Wong R, Loret B, Kent AH (2019) Fully coupled hydro–mechanical controls on non-diffusive seismicity triggering front driven by hydraulic fracturing. *J Seismolog* 23(1):109–121. <https://doi.org/10.1007/s10950-018-9795-0>
- Adachi JI, Detournay E (2008) Plane strain propagation of a hydraulic fracture in a permeable rock. *Eng Fract Mech* 75(16):4666–4694. <https://doi.org/10.1016/j.engfracmech.2008.04.006>
- Barenblatt GI (1959) The formation of equilibrium cracks during brittle fracture: general ideas and hypotheses: axially-symmetric cracks. *J Appl Math Mech* 23(3):622–636
- Bunger AP, Detournay E, Garagash DI (2005) Toughness-dominated hydraulic fracture with leak-off. *Int J Fract* 134(2):175–190. <https://doi.org/10.1007/s10704-005-0154-0>
- Cao W, Younis RM (2023) Formation fracturing by high-energy impulsive mechanical loading. In: SPE reservoir simulation conference. OnePetro
- Cao W, Younis RM. Empirical scaling of formation fracturing by high-energy impulsive mechanical loads. Available at SSRN 4481656
- Carrier B, Granet S (2012) Numerical modeling of hydraulic fracture problem in permeable medium using cohesive zone model. *Eng Fract Mech* 79:312–328. <https://doi.org/10.1016/j.engfracmech.2011.11.012>
- Detournay E (2004) Propagation regimes of fluid-driven fractures in impermeable rocks. *Int J Geomech* 4(1):35–45
- Detournay E, Cheng AH-D (1993) Fundamentals of poroelasticity. In: Analysis and design methods. Elsevier, pp 113–171
- Dugdale D (1960) Yielding of steel sheets containing slits. *J Mech Phys Solids* 8(2):100–104
- Flemisch B, Berre I, Boon W, Fumagalli A, Schwenck N, Scotti A, Stefansson I, Tatomir A (2018) Benchmarks for single-phase flow in fractured porous media. *Adv Water Resour* 111:239–258. <https://doi.org/10.1016/j.advwatres.2017.10.036>
- Fu P, Johnson SM, Carrigan CR (2013) An explicitly coupled hydro-geomechanical model for simulating hydraulic fracturing in arbitrary discrete fracture networks. *Int J Numer Anal Meth Geomech* 37(14):2278–2300
- Garagash DI, Detournay E (2005) Plane-strain propagation of a fluid-driven fracture: small toughness solution
- Geertsma J, De Klerk F (1969) A rapid method of predicting width and extent of hydraulically induced fractures. *J Pet Technol* 21(12):1571–571581
- Haddad M, Sepehrnoori K (2016) XFEM-based CZM for the simulation of 3D multiple-cluster hydraulic fracturing in quasi-brittle shale formations. *Rock Mech Rock Eng* 49(12):4731–4748. <https://doi.org/10.1007/s00603-016-1057-2>
- Haegland H, Assteerawatt A, Dahle HK, Eigestad GT, Helvig R (2009) Comparison of cell- and vertex-centered discretization methods for flow in a two-dimensional discrete-fracture-matrix system. *Adv Water Resour* 32(12):1740–1755. <https://doi.org/10.1016/j.advwatres.2009.09.006>
- Hou J, Qiu M, He X, Guo C, Wei M, Bai B (2016) A dual-porosity-stokes model and finite element method for coupling dual-porosity flow and free flow. *SIAM J Sci Comput* 38(5):B710–B739. <https://doi.org/10.1137/15M1044072>
- Hunsweck MJ, Shen Y, Lew AJ (2013) A finite element approach to the simulation of hydraulic fractures with lag. *Int J Numer Anal Methods Geomech* 37(9):993–1015
- Itasca Consulting Group Ltd (2019) User’s Guide of FLAC3D. Minnesota, USA
- Jiang J, Yang J (2018) Coupled fluid flow and geomechanics modeling of stress-sensitive production behavior in fractured shale gas reservoirs. *Int J Rock Mech Min Sci* 101:1–12. <https://doi.org/10.1016/j.ijrmms.2017.11.003>
- Ju Y, Wang Y, Xu B, Chen J, Yang Y (2019) Numerical analysis of the effects of bedded interfaces on hydraulic fracture propagation in tight multilayered reservoirs considering hydro-mechanical coupling. *J Petrol Sci Eng* 178:356–375. <https://doi.org/10.1016/j.petrol.2019.03.049>
- Karimi-Fard M, Durllofsky LJ (2016) A general gridding, discretization, and coarsening methodology for modeling flow in porous formations with discrete geological features. *Adv Water Resour* 96:354–372. <https://doi.org/10.1016/j.advwatres.2016.07.019>
- Khrstianovic SZY (1955) Formation of vertical fractures by means of highly viscous fluids. Proceeding of the fourth World Petroleum Congress, Section II
- Kresse O, Weng X, Gu H, Wu R (2013) Numerical modeling of hydraulic fractures interaction in complex naturally fractured formations. *Rock Mech Rock Eng* 46(3):555–568. <https://doi.org/10.1007/s00603-012-0359-2>
- Lecampion B, Bunger A (2018) Numerical methods for hydraulic fracture propagation: a review of recent trends. *J Natl Gas Sci Eng* 49:66–83
- Lei Z, Rougier E, Munjiza A, Viswanathan H, Knight EE (2019) Simulation of discrete cracks driven by nearly incompressible fluid via 2D combined finite-discrete element method. *Int J Numer Anal Meth Geomech* 43(9):1724–1743
- Li X-G, Yi L-P, Yang Z-Z, Liu C-y, Yuan P (2017) A coupling algorithm for simulating multiple hydraulic fracture propagation based on extended finite element method. *Environ Earth Sci*. <https://doi.org/10.1007/s12665-017-7092-9>
- Li Y, Liu W, Deng J, Yang Y, Zhu H (2019) A 2D explicit numerical scheme-based pore pressure cohesive zone model for simulating hydraulic fracture propagation in naturally fractured formation. *Energy Sci Eng* 7(5):1527–1543. <https://doi.org/10.1002/ese3.463>
- Lisjak A, Kaifosh P, He L, Tatone BSA, Mahabadi OK, Grasselli G (2017) A 2D, fully-coupled, hydro-mechanical, FDEM formulation for modelling fracturing processes in discontinuous, porous rock masses. *Comput Geotech* 81:1–18. <https://doi.org/10.1016/j.compgeo.2016.07.009>
- Liu G, Sun W, Lowinger SM, Zhang Z, Huang M, Peng J (2018) Coupled flow network and discrete element modeling of injection-induced crack propagation and coalescence in brittle rock. *Acta Geotech* 14(3):843–868. <https://doi.org/10.1007/s11440-018-0682-1>

32. Manzoli OL, Cleto PR, Sánchez M, Guimarães LJN, Maedo MA (2019) On the use of high aspect ratio finite elements to model hydraulic fracturing in deformable porous media. *Comput Methods Appl Mech Eng* 350:57–80. <https://doi.org/10.1016/j.cma.2019.03.006>
33. Mi L, Yan B, Jiang H, An C, Wang Y, Killough J (2017) An Enhanced Discrete Fracture Network model to simulate complex fracture distribution. *J Petrol Sci Eng* 156:484–496. <https://doi.org/10.1016/j.petrol.2017.06.035>
34. Munjiza AA (2004) *The combined finite-discrete element method*. Wiley
35. Munjiza A, Owen D, Bicanic N (1995) A combined finite-discrete element method in transient dynamics of fracturing solids. *Eng Comput* 12(2):145–174
36. Munjiza A, Knight EE, Rougier E (2011) *Computational mechanics of discontinua*. Wiley, London
37. Munjiza A, Knight EE, Rougier E (2015) *Large strain finite element method: a practical course*. Wiley
38. Nordgren R (1972) Propagation of a vertical hydraulic fracture. *Soc Petrol Eng J* 12(04):306–314
39. Perkins T, Kern LR (1961) Widths of hydraulic fractures. *J Petrol Technol* 13(09):937–949
40. Rougier E, Knight EE, Munjiza A (2020) Special issue titled “combined finite discrete element method and virtual experimentation.” *Comput Particle Mech* 7(5):763–763. <https://doi.org/10.1007/s40571-020-00364-z>
41. Salimzadeh S, Usui T, Paluszny A, Zimmerman RW (2017) Finite element simulations of interactions between multiple hydraulic fractures in a poroelastic rock. *Int J Rock Mech Min Sci* 99:9–20. <https://doi.org/10.1016/j.ijrmms.2017.09.001>
42. Song J, Dong M, Koltuk S, Hu H, Zhang L, Azzam R (2018) Hydro-mechanically coupled finite-element analysis of the stability of a fractured-rock slope using the equivalent continuum approach: a case study of planned reservoir banks in Blaubeuren, Germany. *Hydrogeol J* 26(3):803–817. <https://doi.org/10.1007/s10040-017-1694-x>
43. Wang H (2017) Improved dual-porosity models for petrophysical analysis of vuggy reservoirs. *J Geophys Eng* 14(4):758–768
44. Wei D, Zhao B, Gan Y (2022) Surface reconstruction with spherical harmonics and its application for single particle crushing simulations. *J Rock Mech Geotechn Eng* 14(1):232–239. <https://doi.org/10.1016/j.jrmge.2021.07.016>
45. Wu Z, Sun H, Wong LNY (2019) A cohesive element-based numerical manifold method for hydraulic fracturing modelling with Voronoi grains. *Rock Mech Rock Eng* 52(7):2335–2359. <https://doi.org/10.1007/s00603-018-1717-5>
46. Xie L, Min K-B, Shen B (2016) Simulation of hydraulic fracturing and its interactions with a pre-existing fracture using displacement discontinuity method. *J Natl Gas Sci Eng* 36:1284–1294. <https://doi.org/10.1016/j.jngse.2016.03.050>
47. Xu C, Liu Q, Wu J, Deng P, Liu P, Zhang H (2022) Numerical study on P-wave propagation across the jointed rock masses by the combined finite-discrete element method. *Comput Geotechn* 142:104554. <https://doi.org/10.1016/j.compgeo.2021.104554>
48. Yan C et al (2019) A three-dimensional heat transfer and thermal cracking model considering the effect of cracks on heat transfer. *Int J Numer Anal Meth Geomech* 43(10):1825–1853
49. Yan C et al (2019) FDEM-TH3D: a three-dimensional coupled hydrothermal model for fractured rock. *Int J Numer Anal Meth Geomech* 43(1):415–440
50. Yan C et al (2019) A 2D coupled hydro-thermal model for the combined finite-discrete element method. *Acta Geotech* 14(2):403–416
51. Yan C et al (2020) A 2D discrete heat transfer model considering the thermal resistance effect of fractures for simulating the thermal cracking of brittle materials. *Acta Geotech* 15:1303–1319
52. Yan C, Jiao Y-Y (2018) A 2D fully coupled hydro-mechanical finite-discrete element model with real pore seepage for simulating the deformation and fracture of porous medium driven by fluid. *Comput Struct* 196:311–326. <https://doi.org/10.1016/j.compstruc.2017.10.005>
53. Yan C, Ma H et al (2022) A two-dimensional moisture diffusion continuous model for simulating dry shrinkage and cracking of soil. *Int J Geomech* 22(10):04022172
54. Yan C, Tong Y (2020) Calibration of microscopic penalty parameters in the combined finite-discrete element method. *Int J Geomech* 20(7):04020092
55. Yan C, Zheng H (2016) A two-dimensional coupled hydro-mechanical finite-discrete model considering porous media flow for simulating hydraulic fracturing. *Int J Rock Mech Min Sci* 88:115–128. <https://doi.org/10.1016/j.ijrmms.2016.07.019>
56. Yan C, Zheng H (2017) Three-dimensional hydromechanical model of hydraulic fracturing with arbitrarily discrete fracture networks using finite-discrete element method. *Int J Geomech* 17(6):04016133
57. Yan C, Zheng H (2017) FDEM-flow3D: A 3D hydro-mechanical coupled model considering the pore seepage of rock matrix for simulating three-dimensional hydraulic fracturing. *Comput Geotech* 81:212–228. <https://doi.org/10.1016/j.compgeo.2016.08.014>
58. Yan C, Zheng H, Sun G, Ge X (2016) Combined finite-discrete element method for simulation of hydraulic fracturing. *Rock Mech Rock Eng* 49(4):1389–1410. <https://doi.org/10.1007/s00603-015-0816-9>
59. Yan C, Jiao Y-Y, Zheng H (2018) A fully coupled three-dimensional hydro-mechanical finite discrete element approach with real porous seepage for simulating 3D hydraulic fracturing. *Comput Geotech* 96:73–89. <https://doi.org/10.1016/j.compgeo.2017.10.008>
60. Yan X, Huang Z, Yao J, Zhang Z, Liu P, Li Y, Fan D (2019) Numerical simulation of hydro-mechanical coupling in fractured vuggy porous media using the equivalent continuum model and embedded discrete fracture model. *Adv Water Resour* 126:137–154. <https://doi.org/10.1016/j.advwatres.2019.02.013>
61. Yan C, Ren Y, Yang Y (2020) A 3D thermal cracking model for rock based on the combined finite-discrete element method. *Comput Part Mech* 7:881–901
62. Yan C, Fan H, Huang D, Wang G (2021) A 2D mixed fracture-pore seepage model and hydromechanical coupling for fractured porous media. *Acta Geotech*. <https://doi.org/10.1007/s11440-021-01183-z>
63. Yan X, Sun H, Huang Z, Liu L, Wang P, Zhang Q, Yao J (2021) Hierarchical modeling of hydromechanical coupling in fractured shale gas reservoirs with multiple porosity scales. *Energy Fuels* 35(7):5758–5776. <https://doi.org/10.1021/acs.energyfuels.0c03757>
64. Yan C, Tong Y, Luo Z, Ke W, Wang G (2021) A two-dimensional grouting model considering hydromechanical coupling and fracturing for fractured rock mass. *Eng Anal Bound Elem* 133(1):385–397
65. Yan C, Zheng Y, Ke W, Wang G (2021) A FDEM 3D moisture migration-fracture model for simulation of soil shrinkage and desiccation cracking. *Comput Geotech* 140:104425
66. Yan C, Wang T, Ke W, Wang G (2021) A 2D FDEM-based moisture diffusion-fracture coupling model for simulating soil desiccation cracking. *Acta Geotech* 16:2609–2628
67. Yan C, Wang X, Huang D, Wang G (2021) A new 3D continuous-discontinuous heat conduction model and coupled thermo-mechanical model for simulating the thermal cracking of brittle materials. *Int J Solids Struct* 229(15):11123
68. Yan C, Yang Y, Wang G (2021) A new 2D continuous-discontinuous heat conduction model for modeling heat transfer and

- thermal cracking in quasi-brittle materials. *Comput Geotech* 137:104231
69. Yan C, Zheng Y, Huang D, Wang G (2021) A coupled contact heat transfer and thermal cracking model for discontinuous and granular media. *Comput Methods Appl Mech Eng* 375:113587
70. Yan C, Xie X, Ren Y, Ke W (2022) A FDEM-based 2D coupled thermal-hydro-mechanical model for multiphysical simulation of rock fracturing. *Int J Rocj Mech Min Sci* 149:104964
71. Yan C, Wang T, Gao Y, Ke W, Wang G (2022) A three-dimensional grouting model considering hydromechanical coupling based on the combined finite-discrete element method. *Int J Geomech*. [https://doi.org/10.1061/\(ASCE\)GM.1943-5622.0002448](https://doi.org/10.1061/(ASCE)GM.1943-5622.0002448)
72. Yan C, Luo Z, Zheng Y et al (2022) A 2D discrete moisture diffusion model for simulating desiccation fracturing of soil. *Eng Anal Boundary Elem* 138:42–64
73. Yan C, Wei D, Wang G (2022) Three-dimensional finite discrete element-based contact heat transfer model considering thermal cracking in continuous-discontinuous media. *Comput Methods Appl Mech Eng* 388:114228
74. Yan C, Fang H, Zheng Y et al (2022) Simulation of thermal shock of brittle materials using the finite-discrete element method. *Eng Anal Boundary Elem* 115:142–155
75. Yan C, Zhao Z, Yang Y, Zheng H (2023) A three-dimensional thermal-hydro-mechanical coupling model for simulation of fracturing driven by multiphysics. *Comput Geotech* 155:105162
76. Zangeneh N, Eberhardt E, Bustin RM (2015) Investigation of the influence of natural fractures and in situ stress on hydraulic fracture propagation using a distinct-element approach. *Can Geotech J* 52(7):926–946. <https://doi.org/10.1139/cgj-2013-0366>
77. Zhang Q, Borja RI (2021) Poroelastic coefficients for anisotropic single and double porosity media. *Acta Geotech* 16(10):3013–3025. <https://doi.org/10.1007/s11440-021-01184-y>
78. Zhang Q, Wang Z-Y, Yin Z-Y, Jin Y-F (2022) A novel stabilized NS-FEM formulation for anisotropic double porosity media. *Comput Methods Appl Mech Eng* 401:115666. <https://doi.org/10.1016/j.cma.2022.115666>
79. Zhou J, Zhang L, Braun A, Han Z (2017) Investigation of processes of interaction between hydraulic and natural fractures by PFC modeling comparing against laboratory experiments and analytical models. *Energies* 10(7):1001

Publisher's Note Springer Nature remains neutral with regard to jurisdictional claims in published maps and institutional affiliations.

Springer Nature or its licensor (e.g. a society or other partner) holds exclusive rights to this article under a publishing agreement with the author(s) or other rightsholder(s); author self-archiving of the accepted manuscript version of this article is solely governed by the terms of such publishing agreement and applicable law.